Editors' Suggestion | Featured in Physics

Turbulent Nature of the Quasicontinuous Exhaust Regime for Fusion Plasmas

Kaiyu Zhang,* Wladimir Zholobenko, Andreas Stegmeir, Michael Faitsch, Konrad Eder, Christoph Pitzal, Frank Jenko, and ASDEX Upgrade Team†

Max Planck Institute for Plasma Physics, Boltzmannstr. 2, 85748 Garching, Germany

(Received 2 March 2026; accepted 3 June 2026; published 30 July 2026)

We demonstrate a turbulence mechanism that reconciles high plasma confinement with efficient heat exhaust—a central challenge for fusion energy. Global two-fluid turbulence simulations of the reactor-relevant quasicontinuous exhaust regime on the ASDEX Upgrade tokamak reveal that a quasicoherent mode drives mesoscopic oscillations of the pedestal boundary across the magnetic separatrix and ejects ballistic filaments (blobs), reproducing both the mean profiles and turbulent fluctuations observed experimentally. This behavior arises from a synergistic interplay between kinetic ballooning modes and resistive X-point modes straddling the separatrix. These first-principles results place extrapolations to future fusion reactors on a firm physical footing.

DOI: 10.1103/j44y-5dp6

Prospective magnetic confinement fusion reactors must reconcile high energy confinement with tolerable heat exhaust to achieve net gain while protecting plasma-facing components [1]. After years of exploration [2], experiments across multiple tokamaks [3–5] have identified an operational "sweet spot" called the quasicontinuous exhaust (QCE) regime, accessed [6,7] through strong plasma shaping and high plasma density n_{sep} at the magnetic separatrix. QCE integrates H-mode [8] operation with reactor-relevant heat exhaust solutions: Type-I edge-localized modes (ELMs) [9] are naturally suppressed [3], the scrape-off layer (SOL) heat flux decay length λ_q [10] is broadened [11], and the high n_{sep} favors detached operation [12]. These merits are phenomenologically attributed to (i) a quasicoherent mode (QCM) across the separatrix [13–15], whose sufficient transport tailors the pedestal and prevents ELMs, and (ii) intense filamentary blobs [16] in the SOL, whose propagation broadens λ_q [11]. The extrapolation to future devices is hindered by the hitherto unresolved nature of the QCM and blobs, i.e., the generation, interaction, and regulation of those dynamics. A first-principles understanding requires resolving turbulence across the separatrix, where nonlinear, electromagnetic, and intermittent dynamics are further compounded by the transition in magnetic topology.

Here we address the challenge with the two-fluid electromagnetic turbulence code GRILLIX [17–21], well suited for the highly collisional QCE regime. The code adopts a locally field-aligned method [22,23] to maintain

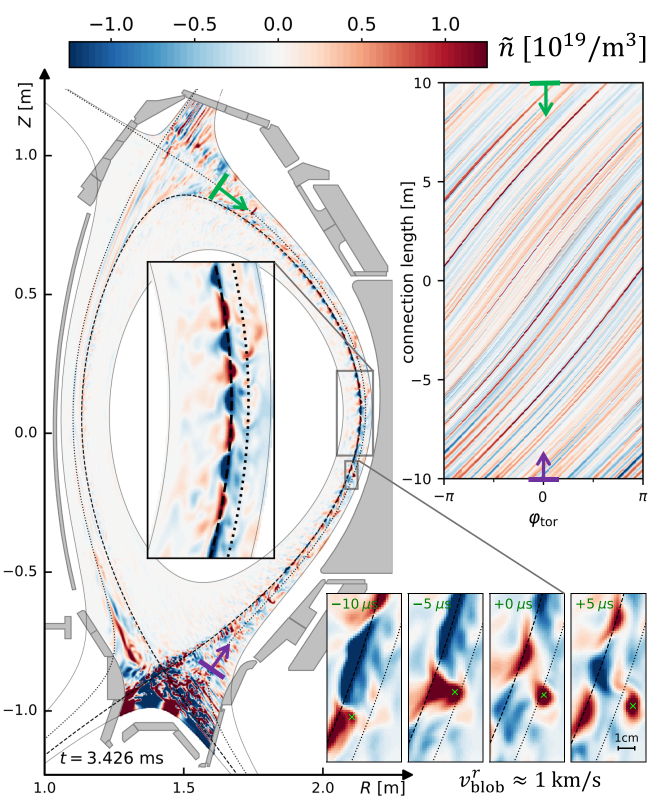

FIG. 1. Composite view of modeled plasma density fluctuations. The color scale is saturated near the divertors. The top-right inset shows toroidal fluctuations; the bottom-right inset shows the time series of the QCM ejecting blobs.

*Contact author: kaiyu.zhang@ipp.mpg.de

†See author list of T. Pütterich *et al.*, 2026 Nucl. Fusion 66 116002 https://doi.org/10.1088/1741-4326/ae61c8.

turbulence-relevant resolution across the separatrix and X point [24]. The background and fluctuating components of plasma quantities evolve together and are fully incorporated into the evolution equations and physical coefficients. Our simulation employs the magnetic equilibrium of the ASDEX Upgrade (AUG) tokamak (QCE discharge No. 36165 at 6.1 s [11]) reproducing the experimentally observed QCM and SOL blobs. Figure 1 illustrates this with density fluctuations $\tilde{n} = n - \bar{n}$, where the overbar denotes a toroidal and time average over the saturated phase, 3.4–3.9 ms, used consistently throughout this Letter. The left panel shows a poloidal cross section of the simulation domain, which includes the separatrix (dashed) and a secondary separatrix (dotted), yielding four parallel boundary regions treated with volume penalization [17,24]. The QCM is localized near the separatrix on the low-field side, displaying sinusoidal fluctuations and a coherent mode structure. At the outboard midplane (OMP), the poloidal wave number is $k_{\mathrm{pol}}\rho_s = 0.033$, within the typical range of QCM measured in AUG [14], where ρ_s is the sound Larmor radius. In the SOL, the outer layer of the QCM launches into blobs, which propagate ballistically into the far-SOL with radial velocity around 1 km/s, consistent with QCE experiments [25]. These blobs have a perpendicular scale of 1 cm and are strongly elongated with parallel extents over 10 m along the magnetic field. This is illustrated by the top-right inset, which shows the fluctuations at the secondary separatrix versus toroidal angle φ_{tor}, with the poloidal coordinate mapped to the connection length to the OMP. Such filamentary structures extend from the OMP to the divertor.

The plasma profiles evolve according to these dynamics and, in the saturated state, agree well with the experiment. Figures 2(a)–2(c) compare the mean density and temperature profiles with experimental integrated data analysis [26] at OMP. Adaptive numerical sources are applied at $\rho_{\mathrm{pol}} < 0.92$ to match the experimental core conditions, whereas a zero-Neumann boundary condition is used at $\rho_{\mathrm{pol}} = 1.06$, allowing the profiles to evolve. The core boundary particle source is negligible in steady state, while the heat source saturates at 3.2 MW. Ionization-recombination sources are obtained by coupling to a three-moment neutral gas model with recycling boundary conditions [27], which results in a high $n_{\mathrm{sep}} = 4 \times 10^{19}/\mathrm{m}^3$ free of *ad hoc* manipulation. For parallel viscosity and heat conduction, we apply neoclassical corrections [20,28,29] and a Landau-fluid closure [30,31], respectively, extending the Braginskii model [32] to a wider range of pedestal collisionalities, while eliminating any free parameters from the model that could otherwise be tuned to adjust the profiles. The first principles profiles of n, T_e, and T_i remain within experimental uncertainty across the edge and SOL. The fluctuation envelope, visualized by the shaded bands, highlights the strong QCM fluctuations at the separatrix and the positively skewed blob statistics in the SOL. Validation extends from the means to the fluctuations.

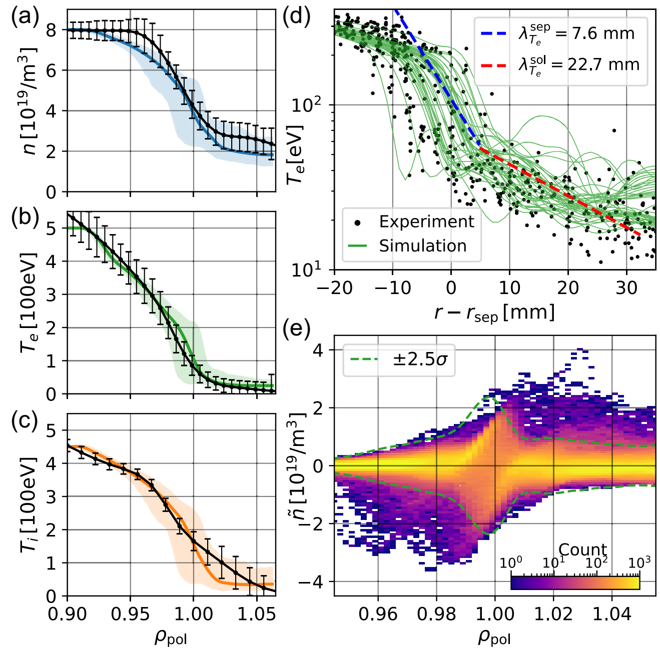

FIG. 2. OMP profiles. (a)–(c) n, T_e, and T_i vs experimental estimates (black markers, error bars indicate uncertainties). Shaded bands show the fluctuation envelope spanning the 1%–99% quantiles. (d) Fluctuating T_e sampled every 0.01 ms over 0.5 ms on a logarithmic y axis, compared to Thomson scattering. The blue and red dashed lines denote linear regressions of the mean T_e in the simulation. (e) Histogram of $\tilde{n}$. The dashed lines mark the $\pm 2.5\sigma$ thresholds.

Figure 2(d) shows instantaneous T_e profiles whose variability agrees well with Thomson scattering measurements at different radii. QCM drives mesoscale radial oscillations of the pedestal foot across the separatrix in the simulation, consistent with the radial spread of the Thomson data at the separatrix. This pattern is reminiscent of the experimental helium beam spectroscopy [25,33], which shows a coherent structure periodically crossing the separatrix.

A key experimental signature of the QCE regime is that the T_e falloff lengths $\lambda_{T_e} = |\partial_r \ln \overline{T_e}|^{-1}$ within and beyond the separatrix are decoupled. This facilitates simultaneous high confinement and heat flux broadening [11] and is shown in Fig. 2(d), where λ_{T_e} appears as linear slopes on a log scale [11,34]. Both experiment and simulation show a distinct SOL decay length (red dashed) that is clearly separated from the near-separatrix decay (blue dashed), the former of which is linked to the presence of blobs. We identify blobs by intermittency: localized, positively skewed density fluctuations exceeding 2.5 standard deviations σ [35]. Figure 2(e) shows probability histograms of $\tilde{n}$ at the OMP. Near the separatrix, the QCM converts fluctuations from negatively skewed distributions for $\rho_{\mathrm{pol}} < 1$ to positively skewed distributions for $\rho_{\mathrm{pol}} > 1$. Away from the separatrix, clear signatures of voids ($< -2.5\sigma$) occur for $\rho_{\mathrm{pol}} < 1$ and blobs ($> 2.5\sigma$) for

$\rho_{\mathrm{pol}} > 1$. Notably, around $\rho_{\mathrm{pol}} = 1.01$ ($r - r_{\mathrm{sep}} = 6.5$ mm), where the QCM terminates, σ drops sharply while the distribution retains a long positive tail. This radius coincides with the blob-launching surface in Fig. 1 and with the beginning of $\lambda_{T_e}^{\mathrm{sol}}$ in Fig. 2(d).

We now investigate the microinstabilities underlying the QCM and blob formation. Figure 3(a) shows the real frequency ω_r versus binormal wave number k_y at $\rho_{\mathrm{pol}} = 0.999$, evaluated in the plasma frame. The dominant branch propagates in the ion diamagnetic direction ($\omega_r < 0$) and follows the theoretical kinetic ballooning mode (KBM) frequency ω_{kbm}. This branch also lies close to $\omega_{*i}/2$, consistent with the experimentally inferred QCM frequency scaling across multiple discharges [14]. A secondary branch propagates weakly in the electron direction ($\omega_r > 0$) and follows the resistive-mode dispersion ω_{resi}. These theoretical dispersions follow from a linear analysis of the two-fluid model in GRILLIX:

$$\omega_{\mathrm{kbm}} = \frac{\frac{1}{6} + \eta_i}{1 + \eta_i}\omega_{*i}, \qquad \omega_{\mathrm{resi}} = \frac{\omega_{*e} + 0.71\eta_e\omega_* + \omega_{*i}}{3}. \qquad (1)$$

Here $\eta_i = L_n/L_{T_i}$, $\eta_e = L_n/L_{T_e}$, $L_n = |\partial_r \ln \overline{n}|^{-1}$, $L_{T_i} = |\partial_r \ln \overline{T_i}|^{-1}$, and $L_{T_e} = |\partial_r \ln \overline{T_e}|^{-1}$. The diamagnetic frequency is $\omega_* = c_s k_y \rho_s / L_n$, with $\omega_{*i} = -(1 + \eta_i)\omega_*$ and $\omega_{*e} = (1 + \eta_e)\omega_*$. The KBM expression differs slightly from the $\omega_{*i}/2$ estimate reported in Ref. [36] due to the inclusion of the time dependence of the ion diamagnetic velocity, $\partial_t \mathbf{u}_*$, in the polarization drift. And ω_{resi} differs from the conventional resistive mode form [37–41] due to the thermal-force contribution $0.71\eta_e\omega_*$ that is included in our model. Equation (1) are obtained asymptotically by truncating higher-order terms in L_n/R_0 (≈ 0.01 in the simulation). In addition, ω_{kbm} assumes the long-wavelength ordering $k_\perp^2 \rho_s^2 \ll 1$, whereas ω_{resi} assumes strong magnetic diffusion, $\omega_\eta = \eta_\parallel k_\perp^2/\mu_0 \gg \omega_*$ with $\eta_\parallel$ being the parallel Spitzer resistivity. Since these orderings constrain $k_\perp$ in opposite ways, they are most simultaneously satisfied in different regions: KBM is favored near the OMP, where $k_\perp \sim k_y$ is relatively small, while the resistive mode is favored closer to the X point, where $k_\perp \gg k_y$ rises sharply due to the diverging connection length. This argument is supported by the results in Figs. 3(b) and 3(c). We first consider the surface $\rho_{\mathrm{pol}} = 0.999$. The KBM, characterized by a kinetic-shear-Alfvén-wave-like [42] anticorrelation between $\tilde{\phi}$ and $\tilde{n}$ [the normalized covariance $c_{\phi,n} = \langle \tilde{\phi}\,\tilde{n} \rangle / (\langle \tilde{\phi}^2 \rangle \langle \tilde{n}^2 \rangle)^{1/2} < 0$, where $\langle \circ \rangle$ denotes the time and toroidal average], dominates at OMP and is progressively stabilized by field-line bending when approaching the X point. Collisionality is insufficient for a resistive ballooning mode to outcompete the KBM at the OMP. Yet resistive drive dominates near the X point due to the rapid growth of $k_\perp$, exciting a resistive X-point mode (RXM) [13,43] with the drift-interchange nature $c_{\phi,n} > 0$.

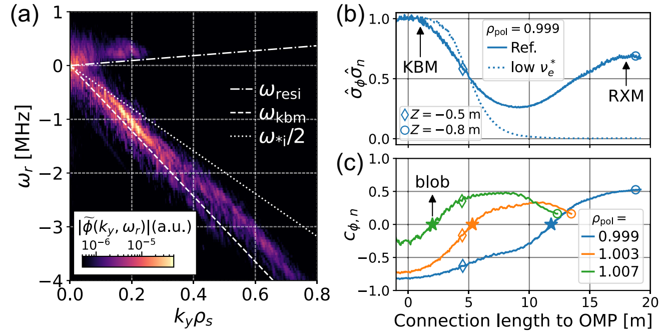

FIG. 3. (a) Binormal Fourier spectra at $\rho_{\mathrm{pol}} = 0.999$ in the plasma frame. The dashed and dash-dotted lines indicate the KBM and RXM dispersion in (1), respectively. (b) Production of fluctuations $\hat{\sigma}_\phi\hat{\sigma}_n$ ($\hat{\sigma}$ is the standard deviation normalized against its value at OMP) at $\rho_{\mathrm{pol}} = 0.999$ as a function of the parallel connection length to OMP, comparing the reference case C1 with lower collisionality. (c) Cross correlation between $\tilde{\phi}$ and $\tilde{n}$, plotted at different flux surfaces. $\Diamond$ and $\circ$ denote the heights $Z = -0.5$ m (where QCM reaches half value) and $Z = -0.8$ m (near the X point), respectively. ☆ marks the zero cross (where interchange occurs).

Importantly, the QCM in Fig. 1 is driven by the KBM rather than the RXM, while blobs are ejected when the RXM interacts with the KBM. The highly shaped equilibrium, an access criterion for QCE, lengthens the parallel connection from OMP to the X-point region, making room for KBM and RXM to coexist on the same flux surface. Inevitably, KBM's and RXM's eigenfunctions with opposite signs of $c_{\phi,n}$ will meet and produce the interchange dynamics $c_{\phi,n} = 0$ at some point [marked by ☆ in Fig. 3(c)]. At $\rho_{\mathrm{pol}} = 0.999$, the interchange coupling occurs close enough to the X point to remain outside the poloidal extent of the QCM's strong-fluctuation region (marked by $\Diamond$). In the SOL, coupling strengthens as the connection length decreases and collisionality increases, shifting the interchange point toward the OMP as ρ_{pol} rises. By $\rho_{\mathrm{pol}} = 1.007$, the interchange lies within the QCM's strong-fluctuation region. Here, $E \times B$ advection efficiently expels the QCM's positive density perturbations outward, launching the blobs seen in Fig. 1 [16,44]. Consistently, a Fourier analysis shows that the phase shift, $\alpha_{\phi,n}(k) = \mathrm{Arg}(\tilde{\phi}_k/\tilde{n}_k)$ with poloidal wave number k, peaks at the QCM poloidal scale near π for $\rho_{\mathrm{pol}} = 0.999$ and gradually decreases to $\pi/2$ for $\rho_{\mathrm{pol}} = 1.007$.

We substantiate the above interpretation with a comparative simulation. Relative to the reference case, we repeat the run with identical parameters except for a reduced neutral density imposed at the divertor plates (case C1). This yields a lower $n_{\mathrm{sep}} = 3 \times 10^{19}/\mathrm{m}^3$ in the saturated state. Case C1 exhibits a QCM similar to Fig. 1 but differs in four aspects. (1) The RXM branch is absent in the Fourier spectrum; only the KBM branch remains, with $\omega_r \approx 1.1\omega_{\mathrm{kbm}}$, higher harmonics, and stronger coherency.

TABLE I. Comparison of key parameters for the reference case (Ref.), the case with same equilibrium but lower n_{sep} (C1), and the case with an ELMy equilibrium (C2). Here n_{sep} is in $[10^{19}\ \mathrm{m}^{-3}]$, and L_c is in [mm]. D^{eff}, χ_e^{eff}, and χ_i^{eff} in $[\mathrm{m}^2/\mathrm{s}]$ are measured at the innermost KBM-unstable ρ_{pol}.

	QCM	Blob	n_{sep}	α_m/α_c	$\nu^*_{e,\mathrm{O}}/\nu^*_{e,\mathrm{X}}$	L_c	D^{eff}	χ_e^{eff}	χ_i^{eff}
Ref.	Yes	Yes	3.9	2.3/2.7	10/28	12	0.27	0.56	1.2
C1	Yes	No	3.0	2.3/2.7	5.2/10	17	0.34	0.70	1.6
C2	No	No	2.2	1.2/2.9	5.3/7.1	5.5	0.12	0.23	0.6

The dotted line in Fig. 3(b) confirms that KBM fluctuations decay toward the X point without the emergence of another mode. (2) The radial profile of the QCM phase shift drops very sharply from $\alpha_{\phi,n} \sim \pi$ to $\alpha_{\phi,n} \sim 0$ at the outmost layer of QCM, without forming a robust interchange spectrum. (3) The SOL is dominated by continuous fluctuations with $\tilde{n} < 2.5\sigma$, with no blob signatures, despite a higher $E \times B$ shear rate in the SOL. (4) T_e exhibits a single exponential decay from the separatrix down to 20 eV in the SOL, with no decoupling between $\lambda_{T_e}^{\mathrm{sep}}$ and $\lambda_{T_e}^{\mathrm{sol}}$. Table I compares key separatrix parameters following [7]: the MHD ballooning parameter $\alpha_m \sim n_{\mathrm{sep}} T_{e,\mathrm{sep}}/\langle\lambda_p\rangle$ ($\langle\circ\rangle$ is the flux-surface average) and the edge collisionality $\nu^*_{e,\mathrm{O}} \sim n_{\mathrm{sep}}/T^2_{e,\mathrm{sep}}$ measured at OMP, and in addition, $\nu^*_{e,\mathrm{X}}$ measured at the orthogonal projection of the X point onto flux surface $\rho_{\mathrm{pol}} = 0.999$. Both cases evolve to nearly identical α_m, close to the ideal-ballooning threshold α_c that is calculated with HELENA for the magnetic equilibrium used here [45]. Poloidally inhomogeneous collisionalities differentiate the two cases. In particular, a threefold lower $\nu^*_{e,\mathrm{X}}$ explains the absence of the RXM in case C1. Overall, case C1 resembles the enhanced D-α regime (EDA) in AUG, featuring a more coherent QCM but weaker blobs [46].

The pedestal-foot transport is primarily set by the KBM nature of the QCM, rather than by a direct collisionality effect or by the RXM. Notably, KBM can also be unstable in the absence of a QCM during the inter-ELM phase [20,47,48]. To examine the difference between inter-ELM KBM and QCM, we include a third simulation C2 based on the inter-ELM phase of an ELMy H-mode equilibrium of AUG No. 40411 [20]. In this case, neither the QCM nor blobs are observed, yet KBM remains at the pedestal foot. Despite similar $k_y\rho_s \approx 0.2$ and $\alpha_{\phi,n} \approx \pi$, the QCMs differ from the inter-ELM KBM by larger radial correlation length L_c [49], shown in Table I. The L_c of QCMs can even exceed the background pressure gradient length $\lambda_p = 8$ mm at the separatrix, enabling mesoscopic heat-transport events from the pedestal to the SOL, in line with the pedestal oscillations in Fig. 2(d) and the streamerlike structures observed experimentally [14,25,33]. The effective particle diffusivity D^{eff} and electron heat conductivity χ_e^{eff} and ion heat conductivity χ_i^{eff} are computed using a Fick-like relation [50]. While Fick coefficients may be insufficient for describing nonlocal KBMs [51,52], they may serve as useful metrics radially inward where KBMs are first destabilized; these are reported in Table I. Transport in the QCM cases is substantially higher than inter-ELM KBM, corroborating the established view that sufficient transport by QCM limits pedestal widening and thereby avoids ELMs [3,6,47]. A detailed comparison yields the transport-strength ordering C1 > Ref. > C2, which clearly tracks L_c rather than the collisionalities. In our model, L_c is limited by $E \times B$ shear, shifting the focus to the radial electric field E_r.

The role of E_r in accessing QCE and avoiding Type-I ELMs has been noted in experiments [33] and MHD simulations [53]; here, we ground this role in first-principles dynamics underlying turbulence self-organization and transport regulation. In our model, E_r is not imposed but evolves through the vorticity dynamics. The radial force balance, $E_r = (\partial_r p_i)/(en) + u_\varphi B_\theta - u_\theta B_\varphi$, is satisfied, where the ion pressure p_i is shaped by transport and the toroidal and poloidal flows (u_φ, u_θ) account for the neoclassical physics [29] and the turbulence effect [54]. In turn, $E \times B$ shear feeds back on the QCM by regulating its L_c and radial location. In the reference simulation, the E_r well at the OMP coincides radially with the peak of the fluctuation intensity of QCM (represented by the square of potential fluctuation $\tilde{\phi}^2$), as shown by the blue curves in Fig. 4. Near the separatrix, E_r is dominated by $(\partial_r p_i)/(en)$, as the flow contributions $u_\theta B_\varphi$ and $u_\varphi B_\theta$ largely cancel. Given $E_r \approx (\partial_r p_i)/(en)$, a high n_{sep} becomes a primary lever for flattening the E_r well and establishing QCM with a large L_c. This may largely explain why n_{sep} appears as a main discriminator between QCE (or EDA) and ELMy operation in experiments [7,55]. Additionally, at fixed n_{sep}, the estimation of L_c is complicated by the $E_r \propto \partial_r p_i$ dependence. The stiffness of $\partial_r p_i$ is determined by the transport whose saturation mechanism entails the zonal flow. The zonally averaged poloidal flow $\langle u_\theta\rangle$ is driven by the flow nonlinearity $\langle\tilde{u}_r\tilde{u}_\theta\rangle$ (Reynolds stress) [56–58]. At high α_m, the zonal flow can be depleted by the magnetic nonlinearity $\langle\tilde{b}_r\tilde{b}_\theta\rangle$ (Maxwell stress) [59,60], which is found to be relevant to the present QCM cases. The QCM efficiently produces Maxwell stress, characterized by the phase shift $\alpha_{b_r,b_\theta} \approx 0$ at the QCM's wave number. This Maxwell stress has a notable impact on the macroscopic profiles. This is confirmed by comparison with a control case derived from the reference case, in which the $\tilde{b}_r\tilde{b}_\theta$ nonlinearity is disabled, shown by orange curves in Fig. 4(a). In this case, while n_{sep} remains essentially unchanged, both E_r and $\partial_r p_i$ evolve much deeper, and the QCM fluctuation vanishes. This outcome can be understood in two steps: (i) without Maxwell-stress depletion, the poloidal-flow contribution $-u_\theta B_\varphi$ exceeds the toroidal one, driving E_r to deviate from $(\partial_r p_i)/(en)$, and (ii) the loss of QCM decreases the transport and steepens the p_i pedestal, further deepening $(\partial_r p_i)/(en)$ and driving the system toward an ELMy-H-mode-like state. We therefore conclude that Maxwell stress is a key component in the self-sustained QCM.

Despite the large fluctuations and long L_c, QCM-driven transport does not fully flatten the pedestal due to $\alpha_{\phi,n} \approx \pi$ (similarly for α_{ϕ,T_e} and α_{ϕ,T_i}). This anticorrelated phase shift, also observed experimentally [61], resembles kinetic-shear-Alfvén-wave oscillations [62] and reduces the efficiency of nonlinear transport. This behavior can be traced to the linear ballooning eigenproblem that governs the KBM, which is derived from the two-fluid model used in GRILLIX and has the form

$$\frac{\mathrm{d}}{\mathrm{d}\theta} f_\theta \frac{\mathrm{d}\Phi}{\mathrm{d}\theta} = \left(C_{0,\theta} + C_{2,\theta}\omega^2 + C_{1,\theta}\omega + \frac{C_{-1,\theta}}{\omega - \omega_1} \right)\Phi, \qquad (2)$$

where $\Phi = \tilde{A}_{\|,\mathbf{k}}/(k_\| R_0)$ is the Fourier eigenfunction to be solved, $\omega = \omega_r + \gamma i$ is the complex eigenfrequency, and θ is the ballooning angle [63]. $f_\theta = 1 + (s\theta - \alpha_m \sin\theta)^2$ is a function of θ depending on α_m and the magnetic shear s. Inside the bracket is a polynomial of ω^j with the prefactor $C_{j,\theta}$, which assembles the key physics determining the instability of the system. The $C_{0,\theta}$ and $C_{2,\theta}$ terms recover the ideal ballooning mode [63], which has a quadratic form of ω and hence $\omega_r = 0$ and the approximated interchange-like phase shift $\alpha_{\phi,n} \approx \arg(\omega) = \pi/2$. The $C_{-1,\theta}$ term represents the ion magnetic drift resonance, originating from the ion's perpendicular heat conduction as a two-fluid effect in toroidal geometry, and destabilizes the system by reducing α_m threshold given a high η_i. Importantly, the $C_{1,\theta}$ term arises from retaining $(\partial_t + \mathbf{u}_E \cdot \nabla)\mathbf{u}_*$ in the polarization drift, representing the finite-Larmor-radius (FLR) effects. Its inclusion introduces a significant real frequency component $\omega_r = \omega_{\mathrm{kbm}} < 0$ consistent with [36]. Consequently, when KBM is marginally unstable, we expect $\alpha_{\phi,n} \approx \pi$ for $\gamma \ll |\omega_{\mathrm{kbm}}|$. The significance of FLR physics in KBM turbulence is further substantiated by a no-FLR control case derived from the reference case, where the term $(\mathbf{u}_E \cdot \nabla)\mathbf{u}_*$ is removed from the polarization drift. Fig. 4(b) shows the cross-coherence between $\tilde{\phi}$ and $\tilde{n}$ at $\rho_{\mathrm{pol}} = 0.999$ near the OMP for comparison. The probability density increases linearly from the outer to the inner contours. When FLR is removed, the picture shifts from a coherent pattern aligned diagonally ($\alpha_{\phi,n} \approx \pi$) to broadband turbulence aligned horizontally ($\alpha_{\phi,n} \approx \pi/2$). The no-FLR case, subject to interchangelike dynamics, exhibits a tenfold increase in $E \times B$ heat flux, leading to pedestal collapse and thus discrepancy with the experiment. These results underscore that FLR stabilization is essential for sustaining the coherent QCM structure with $\alpha_{\phi,n} \approx \pi$, and for preventing its transport from degrading the confinement.

To summarize, validated simulations reveal the turbulent nature of the quasicontinuous exhaust regime, a promising scenario for fusion reactors. The experimentally observed QCM and blob dynamics, reproduced in the simulations, are governed by two separatrix-spanning modes. The QCM is a kinetic ballooning mode (KBM) that develops an extended, mesoscopic radial correlation length via electromagnetic self-organization of turbulence, thereby driving enhanced transport. Blob launching occurs via interchange dynamics when this upstream KBM activity interacts with a resistive mode originating from the X-point region (RXM).

This Letter provides a sound physics basis for extrapolations to future reactors. Our results suggest, first, that access to the KBM-dominated QCM should depend primarily on the beta-related ballooning parameter [5,6], rather than on collisionality-related parameters [64–66] as assumed in extrapolations based on resistivity-dominated modes [7]. However, the experimentally observed separatrix density dependence [7,55] may instead reflect the requirement for reduced $E \times B$ shear. Quantitatively predicting whether QCM transport is sufficient to suppress ELMs, yet not so excessive as to degrade confinement, will require parameterizing the $E \times B$ shear weakening by Maxwell stress and interchange stabilization by finite-Larmor-radius physics, respectively. Second, blob-enhanced exhaust requires the coexistence of those KBMs with an RXM destabilized by elevated local collisionality near the X point, rather than the excitation of a resistive ballooning mode by high upstream collisionality. Thus, despite the more constrained access to high outboard-midplane separatrix collisionality in reactor-scale devices such as ITER [4,5], the mechanisms elucidated herein may nevertheless remain applicable for reconciling high confinement with effective heat exhaust in future fusion plasmas.

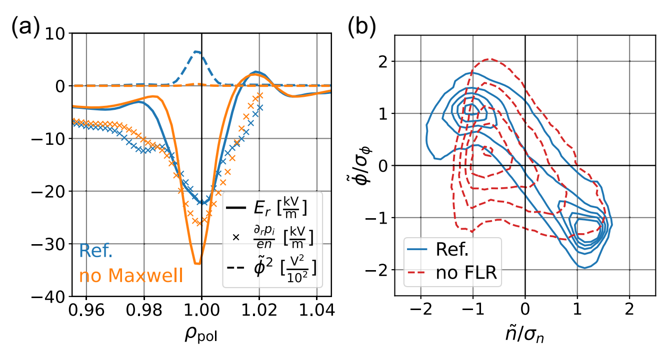

FIG. 4. (a) Mean profiles of E_r, $(\partial_r p_i)/(en)$ and $\tilde{\phi}^2$, comparing the reference case and the test where the Maxwell stress is removed. (b) Cross coherence between $\tilde{\phi}$ and $\tilde{n}$, comparing the reference case and the test without FLR.

Acknowledgments—The authors would like to thank P. Manz, T. Pütterich, G. Birkenmeier, M. Dunne, A. Cathey, P. Ulbl, J. Kalis, J. Pfennig, L. Radovanovic, and B. Frei for fruitful discussions on many intricate topics. This work received funding from the German Federal Ministry of Research, Technology and Space (BMFTR) within the funding program Fusion 2040 (Reference No. 13F1046). This work was carried out within the framework of the EUROfusion Consortium, funded by the European Union via the Euratom Research and Training Programme (Grant Agreement No. 101052200—EUROfusion). The simulations were performed on the national supercomputer HPE Apollo Hawk at the High Performance Computing Center Stuttgart (HLRS) under Grant No. GRILLIX/44281.

The views and opinions expressed are however those of the author(s) only and do not necessarily reflect those of the European Union or the European Commission. Neither the European Union nor the European Commission can be held responsible for them.

Data availability—The data that support the findings of this article are not publicly available upon publication because it is not technically feasible and/or the cost of preparing, depositing, and hosting the data would be prohibitive within the terms of this research project. The data are available from the authors upon reasonable request.

[1] M. Siccinio, W. Biel, M. Cavedon *et al.*, Fusion Eng. Des. **156**, 111603 (2020).
[2] E. Viezzer, Nucl. Fusion **58**, 115002 (2018).
[3] G. Harrer, E. Wolfrum, M. Dunne, P. Manz, M. Cavedon, P. Lang, B. Kurzan, T. Eich, B. Labit, J. Stober *et al.*, Nucl. Fusion **58**, 112001 (2018).
[4] B. Labit, T. Eich, G. F. Harrer, E. Wolfrum, M. Bernert, M. Dunne, L. Frassinetti, P. Hennequin, R. Maurizio, A. Merle *et al.*, Nucl. Fusion **59**, 086020 (2019).
[5] M. Faitsch, M. Dunne, E. Lerche, P. Lomas, I. Balboa, P. Bilkova, P. Bohm, A. Kappatou, D. Kos, B. Labit *et al.*, Nucl. Fusion **65**, 024003 (2025).
[6] M. Dunne, M. Faitsch, L. Radovanovic, E. Wolfrum, and ASDEX Upgrade Team, Nucl. Fusion **64**, 124003 (2024).
[7] M. Faitsch, T. Eich, G. Harrer, E. Wolfrum, D. Brida, P. David, M. Dunne, L. Gil, B. Labit, U. Stroth *et al.*, Nucl. Fusion **63**, 076013 (2023).
[8] F. Wagner, G. Becker, K. Behringer *et al.*, Phys. Rev. Lett. **49**, 1408 (1982).
[9] H. Zohm, Plasma Phys. Controlled Fusion **38**, 105 (1996).
[10] T. Eich *et al.*, Nucl. Fusion **53**, 093031 (2013).
[11] M. Faitsch, T. Eich, G. Harrer, E. Wolfrum, D. Brida, P. David, M. Griener, U. Stroth, A. U. Team, E. M. Team *et al.*, Nucl. Mater. Energy **26**, 100890 (2021).
[12] M. Wischmeier and ASDEX Upgrade Team, J. Nucl. Mater. **463**, 22 (2015).
[13] A. Mazurenko, M. Porkolab, D. Mossessian, J. A. Snipes, X. Q. Xu, and W. M. Nevins, Phys. Rev. Lett. **89**, 225004 (2002).
[14] J. Kalis, G. Birkenmeier, P. Manz, T. Eich, M. Griener, R. Goti, M. Cavedon, L. Gil, M. Faitsch, L. Radovanovic *et al.*, Nucl. Fusion **64**, 016038 (2023).
[15] J. Terry, N. Basse, I. Cziegler, M. Greenwald, O. Grulke, B. LaBombard, S. Zweben, E. Edlund, J. Hughes, L. Lin *et al.*, Nucl. Fusion **45**, 1321 (2005).
[16] D. D'ippolito, J. Myra, and S. Zweben, Phys. Plasmas **18**, 060501 (2011).
[17] A. Stegmeir, A. Ross, T. Body, M. Francisquez, W. Zholobenko, D. Coster, O. Maj, P. Manz, F. Jenko, B. Rogers *et al.*, Phys. Plasmas **26**, 052517 (2019).
[18] K. Zhang, W. Zholobenko, A. Stegmeir, K. Eder, and F. Jenko, Nucl. Fusion **64**, 036016 (2024).
[19] K. Zhang, W. Zholobenko, A. Stegmeir, K. Eder, and F. Jenko, Comput. Phys. Commun. **314**, 109670 (2025).
[20] W. Zholobenko, K. Zhang, A. Stegmeir, J. Pfennig, K. Eder, C. Pitzal, P. Ulbl, M. Griener, L. Radovanovic and U. Plank, Nucl. Fusion **64**, 106066 (2024).
[21] W. Zholobenko, F. Jenko, K. Zhang, P. Ulbl, K. Eder, A. Stegmeir, C. Angioni, and P. Manz, Phys. Rev. Lett. **136**, 075101 (2026).
[22] A. Stegmeir, D. Coster, O. Maj, K. Hallatschek, and K. Lackner, Comput. Phys. Commun. **198**, 139 (2016).
[23] A. Stegmeir, O. Maj, D. Coster, K. Lackner, M. Held, and M. Wiesenberger, Comput. Phys. Commun. **213**, 111 (2017).
[24] A. Stegmeir, T. Body, and W. Zholobenko, Comput. Phys. Commun. **290**, 108801 (2023).
[25] M. Griener, E. Wolfrum, G. Birkenmeier, M. Faitsch, R. Fischer, G. Fuchert, L. Gil, G. Harrer, P. Manz, D. Wendler, and U. Stroth, Nucl. Mater. Energy **25**, 100854 (2020).
[26] R. Fischer, C. Fuchs, B. Kurzan, W. Suttrop, E. Wolfrum, and A. U. Team, Fusion Sci. Technol. **58**, 675 (2010).
[27] K. Eder, A. Stegmeir, W. Zholobenko, J. Pfennig, D. Brida, G. Grenfell, F. Jenko, and ASDEX Upgrade Team, Plasma Phys. Controlled Fusion **67**, 065034 (2025).
[28] S. Hirshman and D. Sigmar, Nucl. Fusion **21**, 1079 (1981).
[29] V. Rozhansky, E. Kaveeva, P. Molchanov, I. Veselova, S. Voskoboynikov, D. Coster, G. Counsell, A. Kirk, S. Lisgo (The ASDEX-Upgrade Team and The MAST Team), Nucl. Fusion **49**, 025007 (2009).
[30] G. W. Hammett and F. W. Perkins, Phys. Rev. Lett. **64**, 3019 (1990).
[31] C. Pitzal, A. Stegmeir, W. Zholobenko, K. Zhang, and F. Jenko, Phys. Plasmas **30**, 122502 (2023).
[32] S. Braginskii, Rev. Plasma Phys. **1**, 205 (1965).
[33] G. F. Harrer, M. Faitsch, L. Radovanovic, E. Wolfrum, C. Albert, A. Cathey, M. Cavedon, M. Dunne, T. Eich, R. Fischer, M. Griener, M. Hoelzl, B. Labit, H. Meyer, F. Aumayr (The Asdex Upgrade Team, and The EUROfusion MST1 Team), Phys. Rev. Lett. **129**, 165001 (2022).
[34] H. J. Sun, E. Wolfrum, T. Eich, B. Kurzan, S. Potzel, U. Stroth and ASDEX Upgrade Team, Plasma Phys. Controlled Fusion **57**, 125011 (2015).
[35] P. Manz, T. Ribeiro, B. Scott, G. Birkenmeier, D. Carralero, G. Fuchert, S. Müller, H. Müller, U. Stroth, and E. Wolfrum, Phys. Plasmas **22**, 022308 (2015).
[36] K. Aleynikova and A. Zocco, Phys. Plasmas **24**, 092106 (2017).

[37] G. Ara, B. Basu, B. Coppi, G. Laval, M. Rosenbluth, and B. Waddell, Ann. Phys. (N.Y.) **112**, 443 (1978).
[38] F. Porcelli and S. Migliuolo, Phys. Fluids **29**, 1741 (1986).
[39] M. Kotschenreuther, X. Liu, D. Hatch, S. Mahajan, L. Zheng, A. Diallo, R. Groebner, J. Hillesheim, C. Maggi, C. Giroud *et al.*, Nucl. Fusion **59**, 096001 (2019).
[40] S. Gupta, J. D. Callen, and C. C. Hegna, Phys. Plasmas **9**, 3395 (2002).
[41] J. Myra and D. D'Ippolito, Phys. Plasmas **12**, 092511 (2005).
[42] H. Doerk, C. Challis, J. Citrin, J. Garcia, T. Görler, F. Jenko, and J. Contributors, Plasma Phys. Controlled Fusion **58**, 115005 (2016).
[43] J. R. Myra, D. A. D'Ippolito, X. Q. Xu, and R. H. Cohen, Phys. Plasmas **7**, 2290 (2000).
[44] S. I. Krasheninnikov, Phys. Lett. A **283**, 368 (2001).
[45] L. Radovanovic, M. Dunne, E. Wolfrum, G. Harrer, M. Faitsch, R. Fischer, and F. Aumayr, Nucl. Fusion **62**, 086004 (2022).
[46] L. Gil, C. Silva, T. Happel, G. Birkenmeier, G. D. Conway, L. Guimarais, A. Kallenbach, T. Pütterich, J. Santos, P. A. Schneider *et al.*, Nucl. Fusion **60**, 054003 (2020).
[47] P. Snyder, R. Groebner, J. Hughes, T. Osborne, M. Beurskens, A. Leonard, H. Wilson, and X. Xu, Nucl. Fusion **51**, 103016 (2011).
[48] D. Dickinson, C. M. Roach, S. Saarelma, R. Scannell, A. Kirk, and H. R. Wilson, Phys. Rev. Lett. **108**, 135002 (2012).
[49] J. Wesson and D. J. Campbell, *Tokamaks*, 4th ed., Oxford Science Publications No. 149 (Oxford University Press, New York, 2011).
[50] J. Callen, R. Groebner, T. Osborne, J. Canik, L. W. Owen, A. Pankin, T. Rafiq, T. Rognlien, and W. Stacey, Nucl. Fusion **50**, 064004 (2010).
[51] T. Hahm and P. Diamond, J. Korean Phys. Soc. **73**, 747 (2018).
[52] A. Ashourvan and P. H. Diamond, Phys. Rev. E **94**, 051202 (2016).
[53] A. Cathey, M. Hoelzl, G. Harrer, M. Dunne, G. Huijsmans, K. Lackner, S. Pamela, E. Wolfrum, S. Günter and JOREK team, Plasma Phys. Controlled Fusion **64**, 054011 (2022).
[54] P. Diamond and Y.-B. Kim, Phys. Fluids B **3**, 1626 (1991).
[55] M. A. Miller, J. W. Hughes, T. Eich, G. R. Tynan, P. Manz, T. Body, D. Silvagni, O. Grover, A. E. Hubbard, A. Cavallaro *et al.*, Nucl. Fusion **65**, 052002 (2025).
[56] A. Smolyakov, P. Diamond, and M. Medvedev, Phys. Plasmas **7**, 3987 (2000).
[57] W. Zholobenko, T. Body, P. Manz, A. Stegmeir, B. Zhu, M. Griener, G. D. Conway, D. Coster, and F. Jenko, Plasma Phys. Controlled Fusion **63**, 034001 (2021).
[58] P. H. Diamond, S. Itoh, K. Itoh, and T. Hahm, Plasma Phys. Controlled Fusion **47**, R35 (2005).
[59] B. D. Scott, New J. Phys. **7**, 92 (2005).
[60] V. Naulin, A. Kendl, O. Garcia, A. Nielsen, and J. J. Rasmussen, Phys. Plasmas **12**, 052515 (2005).
[61] G. Grenfell, L. Gil, P. Manz, C. Silva, J. Adamek, D. Brida, G. Conway, T. Eich, M. Faitsch, T. Happel *et al.*, Nucl. Fusion **64**, 104002 (2024).
[62] B. Scott, *Turbulence and Instabilities in Magnetised Plasmas, Volume 1: Fluid Drift Turbulence* (IOP Publishing, Bristol, UK, 2021), 10.1088/978-0-7503-2504-2.
[63] J. W. Connor, R. J. Hastie, and J. B. Taylor, Phys. Rev. Lett. **40**, 396 (1978).
[64] A. Zeiler, D. Biskamp, J. F. Drake, and B. N. Rogers, Phys. Plasmas **5**, 2654 (1998).
[65] B. D. Scott, Phys. Plasmas **12**, 062314 (2005).
[66] T. Eich, P. Manz, R. Goldston, P. Hennequin, P. David, M. Faitsch, B. Kurzan, B. Sieglin, E. Wolfrum, and ASDEX Upgrade Team, Nucl. Fusion **60**, 056016 (2020).